LETTERS
PUBLISHED ONLINE: 18 JULY 2010 | DOI: 10.1038/NMAT2800
nature materials

From (π,0) magnetic order to superconductivity with (π,π) magnetic resonance in $Fe_{1.02}Te_{1-x}Se_x$

T. J. Liu[1], J. Hu[1], B. Qian[1], D. Fobes[1], Z. Q. Mao[1]*, W. Bao[2]*, M. Reehuis[3], S. A. J. Kimber[3], K. Prokeš[3], S. Matas[3], D. N. Argyriou[3], A. Hiess[4], A. Rotaru[5], H. Pham[5], L. Spinu[5], Y. Qiu[6,7], V. Thampy[8], A. T. Savici[8,9], J. A. Rodriguez[6,7,8] and C. Broholm[6,8]

The iron chalcogenide $Fe_{1+y}(Te_{1-x}Se_x)$ is structurally the simplest of the Fe-based superconductors[1–3]. Although the Fermi surface is similar to iron pnictides[4,5], the parent compound $Fe_{1+y}Te$ exhibits antiferromagnetic order with an in-plane magnetic wave vector (π,0) (ref. 6). This contrasts the pnictide parent compounds where the magnetic order has an in-plane magnetic wave vector (π,π) that connects hole and electron parts of the Fermi surface[7,8]. Despite these differences, both the pnictide and chalcogenide Fe superconductors exhibit a superconducting spin resonance around (π,π) (refs 9–11). A central question in this burgeoning field is therefore how (π,π) superconductivity can emerge from a (π,0) magnetic instability[12]. Here, we report that the magnetic soft mode evolving from the (π,0)-type magnetic long-range order is associated with weak charge carrier localization. Bulk superconductivity occurs as magnetic correlations at (π,0) are suppressed and the mode at (π,π) becomes dominant for $x > 0.29$. Our results suggest a common magnetic origin for superconductivity in iron chalcogenide and pnictide superconductors.

Unconventional superconductivity in cuprates, heavy-fermion intermetallics and strontium ruthenate all occur in close proximity to magnetic instabilities and seem to be mediated by spin fluctuations. The newly discovered iron pnictide superconductors[13–16] follow the paradigm of superconductivity achieved by suppressing a long-range magnetic order through charge carrier doping or pressure. The long-range antiferromagnetic (AFM) order in the parent compounds of iron pnictide superconductors is characterized by the in-plane Fermi surface nesting wave vector $Q_n = (\pi,\pi)$ (refs 7,8). (Here and throughout this Letter, we refer to wave vectors in units of the inverse tetragonal lattice parameters.) Iron chalcogenide $Fe_{1+y}(Te_{1-x}Se_x)$ superconductors, discovered more recently[1–3], have a similar Fermi surface to iron pnictides, according to both density functional calculations[4] and photoemission measurements[5]. However, the undoped parent compound of this system, $Fe_{1.02}Te$, exhibits AFM order characterized by an in-plane wave vector $Q_m = (\pi,0)$ (ref. 6), which distinguishes this compound from the iron pnictide parent materials. Yet both doped iron chacolgenide[11] and iron pnictide[9,10] superconductors exhibit a magnetic resonance in the spin excitation spectra below T_c around the wave vector (π,π) consistent with $s_\pm$ pairing symmetry[17–19]. Resolution of the dichotomy between (π,0) magnetic order in undoped FeTe and superconductivity with (π,π) magnetic resonance in Se-doped samples is a key challenge to our emerging understanding of iron-based superconductivity[12].

Here, we address the challenge through systematic investigation of transport, magnetic and superconducting properties in various regions of the phase diagram of $Fe_{1.02}(Te_{1-x}Se_x)$ using resistivity, Hall coefficient, magnetic susceptibility, specific heat and neutron scattering measurements. We find that magnetic correlations of the (π,0) variety survive as short-range magnetic correlations after the long-range AFM phase has been suppressed by partial Se substitution for Te. Our results link these correlations to weak charge carrier localization in underdoped samples. Bulk superconductivity occurs only when magnetic correlations near (π,0), although still present, are strongly suppressed and spin fluctuations near (π,π) become dominant for $x > 0.29$. The latter exhibit a spin gap and a spin resonance in the superconducting state. These results indicate that short-range magnetic correlations near (π,0) are antagonistic to metallicity and superconductivity, and that iron chalcogenide and iron pnictide superconductivity have similar origins associated with (π,π) spin fluctuations.

Using a variety of techniques we have constructed a detailed electronic and magnetic phase diagram of $Fe_{1.02}(Te_{1-x}Se_x)$ with $0 \leq x < 0.5$, which is shown in Fig. 1a. In summary, we find three composition regions with distinct physical properties. Region I ($0 \leq x < 0.09$) exhibits long-range AFM order with a wave vector (π,0). Region II ($0.09 < x < 0.29$) exhibits neither long-range AFM order nor bulk superconductivity. Only in region III ($x \geq 0.29$) do we find evidence of bulk superconductivity. More specifically in Fig. 1a, the squares, downtriangles, uptriangles and crosses represent the Néel temperatures T_N determined by neutron diffraction, d.c. susceptibility, Hall coefficient and resistivity measurements, respectively. Importantly, these disparate measurements are entirely consistent with each other. T_N gradually decreases with increasing Se content, approaching zero for $x \sim 0.09$. A trace of superconductivity is observed for $0.04 \leq x < 0.09$, which will be examined in greater detail later as a non-bulk phenomenon. The open diamonds represent the onset of the superconducting transition T_c^ρ as indicated by the resistivity data. In region II ($0.09 < x < 0.29$), although long-range AFM order is fully suppressed, non-bulk superconductivity remains with a volume fraction, V_{SC}, that is less than 3% for all samples with

[1]Department of Physics and Engineering Physics, Tulane University, New Orleans, Louisiana 70118, USA, [2]Department of Physics, Renmin University of China, Beijing 100872, China, [3]Helmholtz-Zentrum Berlin für Materialen und Energie, Hahn-Meitner Platz 1, D-14109 Berlin, Germany, [4]Institut Max von Laue-Paul Langevin, 6 rue Jules Horowitz, BP 156, F-38042, Grenoble Cedex 9, France, [5]Advanced Materials Research Institute and Department of Physics, University of New Orleans, New Orleans, Louisiana 70148, USA, [6]NIST Center for Neutron Research, National Institute of Standards and Technology, Gaithersburg, Maryland 20899, USA, [7]Department of Materials Science and Engineering, University of Maryland, College Park, Maryland 20899, USA, [8]Institute for Quantum Matter and Department of Physics and Astronomy, The Johns Hopkins University, Baltimore, Maryland 21218, USA, [9]NSSD, Oak Ridge National Laboratory, Oak Ridge, Tennessee 37831, USA. *e-mail: zmao@tulane.edu; wbao@ruc.edu.cn.

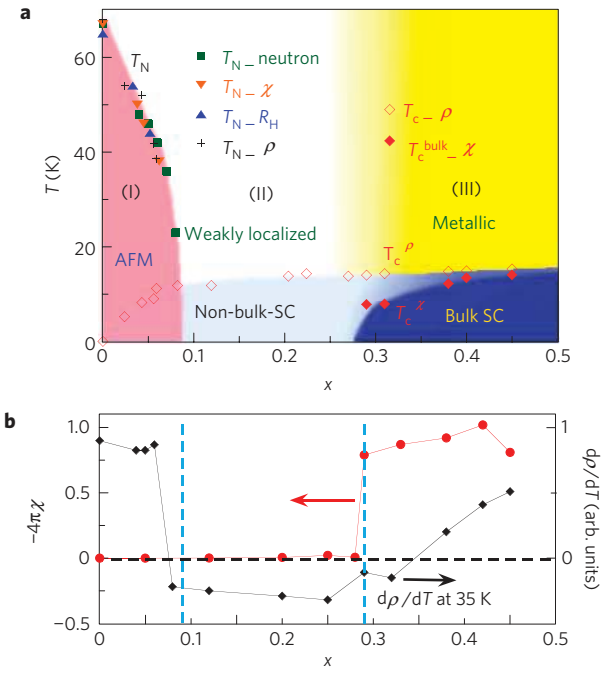

Figure 1 | Magnetic and superconducting properties of $Fe_{1.02}(Te_{1-x}Se_x)$ ($0 \le x < 0.5$). **a**, The phase diagram. The Néel temperature, T_N, of the AFM phase, determined by neutron scattering (green squares), susceptibility (orange triangles), Hall coefficient (blue triangles) and resistivity (black crosses) measurements. T_c^{ρ}, onset of the superconducting transition probed by resistivity (open diamonds); T_c^{χ}, bulk superconducting transition temperature (filled diamonds) probed by susceptibility. Bulk superconductivity (SC) exists when sufficient Te is replaced by Se, with the superconducting volume fraction >75% for $x \ge 0.29$. For $x < 0.29$, only non-bulk-superconductivity exists with the superconducting volume fraction <3%. The bulk superconductivity and non-bulk superconductivity concentration regions also differ in their normal-state transport property: metallic in the former, non-metallic in the latter. **b**, The superconducting volume fraction ($-4\pi\chi$) and the derivative of normalized resistivity ($\rho(T)/\rho(300\,\mathrm{K})$) with respect to temperature as a function of Se content.

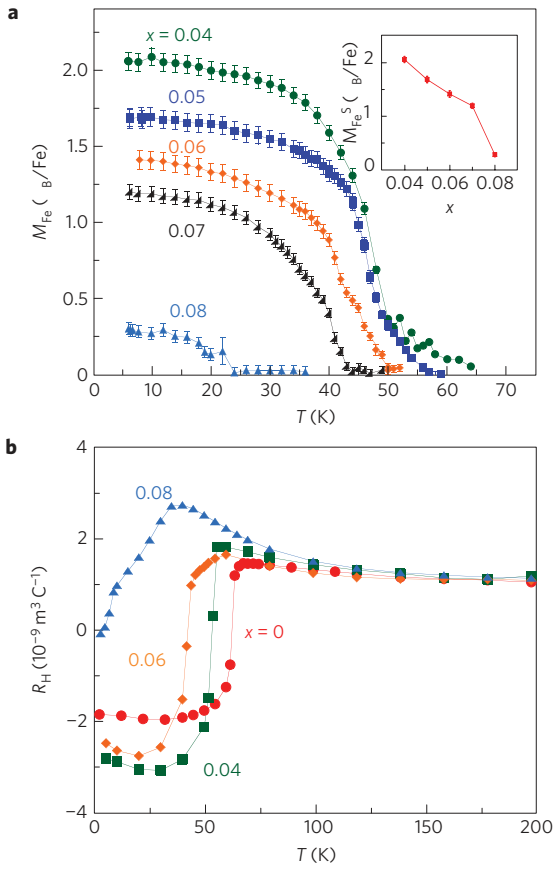

Figure 2 | Evolution of the long-range AFM order and Fermi-surface variation across the AFM transition in $Fe_{1.02}(Te_{1-x}Se_x)$. **a**, Temperature dependence of the ordered magnetic moment M_{Fe}. Inset: The saturated moment M_{Fe} as a function of Se content. The magnetic order is suppressed when $x > 0.09$. **b**, Hall coefficients as a function of temperature. The Fermi surface changes significantly across the AFM transition.

$x < 0.29$. In region III ($x \ge 0.29$), however, bulk superconductivity is found. The filled diamonds represent the bulk superconducting transition temperature T_c^{χ} probed by susceptibility. V_{SC} rises to above 75% for $x \ge 0.29$, as shown in Fig. 1b. In region II, the transport properties above T_c^{ρ} indicate weak charge carrier localization, which contrasts with the metallic behaviour seen in the normal state of region III and the AFM phase of region I. The cross-over is clearly indicated by the sign change in the derivative of resistivity with respect to temperature $d\rho/dT$ (see Fig. 1b). The absence of bulk superconductivity in region II makes the phase diagram of $Fe_{1.02}(Te_{1-x}Se_x)$ distinct from those of iron pnictide superconductors where bulk superconductivity either appears immediately following suppression of long-range AFM order[20,21], or coexists with (π,π) AFM order in a certain composition range[22–24].

We shall now address properties of each region of the phase diagram (Fig. 1a) in greater detail. Throughout the AFM phase (region I), elastic neutron scattering measurements reveal the same commensurate $(\pi,0)$ magnetic structure as reported for the parent compound[6]. The ordered magnetic moment of iron M_{Fe} depends strongly on the Se content as shown in Fig. 2a. M_{Fe} is approximately 2.09(3) μ_B/Fe for the $x = 0.04$ sample, but decreases to 0.33(2) μ_B/Fe for $x = 0.08$. The saturated staggered magnetic moment for $Fe_{1.02}Te$ (ref. 6) is much larger than that of iron pnictide parent compounds (0.36 μ_B/Fe for LaOFeAs (ref. 7) and 0.87 μ_B/Fe for $BaFe_2As_2$ (ref. 8)). The Hall effect measurements shown in Fig. 2b indicate that the AFM transition in region I is accompanied by a remarkable change of the Fermi surface. For $x < 0.08$ the Hall coefficient R_H exhibits a sharp drop from a positive to a negative value across the transition. This indicates that the Fermi surface is dominated by holes above T_N and by electrons below T_N.

Figure 3a presents the in-plane resistivity $\rho_{ab}(T)$ as a function of temperature for typical samples in region I. $\rho_{ab}(T)$ exhibits an anomaly at T_N, which is marked by a downward arrow in the figure. Each sample in this region also shows a trace of superconductivity below the AFM transition. This can be seen from the second drop of $\rho_{ab}(T)$ at low temperatures (denoted by upward arrows in Fig. 3a). Although T_c^{ρ} shows a systematic increase with increasing Se content in this region, the superconducting volume fraction is nearly zero (Figs 1b and 3d) because we did not observe any diamagnetism below T_c^{ρ} for these samples (see Fig. 3d).

Despite the complete suppression of long-range AFM order, superconductivity remains a non-bulk phenomenon throughout region II. Although all samples in this region exhibit zero resistance below T_c^{ρ}, their susceptibility fails to exhibit significant diamagnetism when the resistivity vanishes (Figs 1b and 3d). The superconducting volume fraction of these samples estimated from $-4\pi\chi$ is below 3%. Furthermore, the specific heats of samples in both regions I and II are free of anomalies near the resistive superconducting transition. They can approximately be described by $C = \gamma T + \beta T^3$ at low temperatures, where γT and βT^3 represent the electron and phonon specific heat, respectively. Figure 3e shows

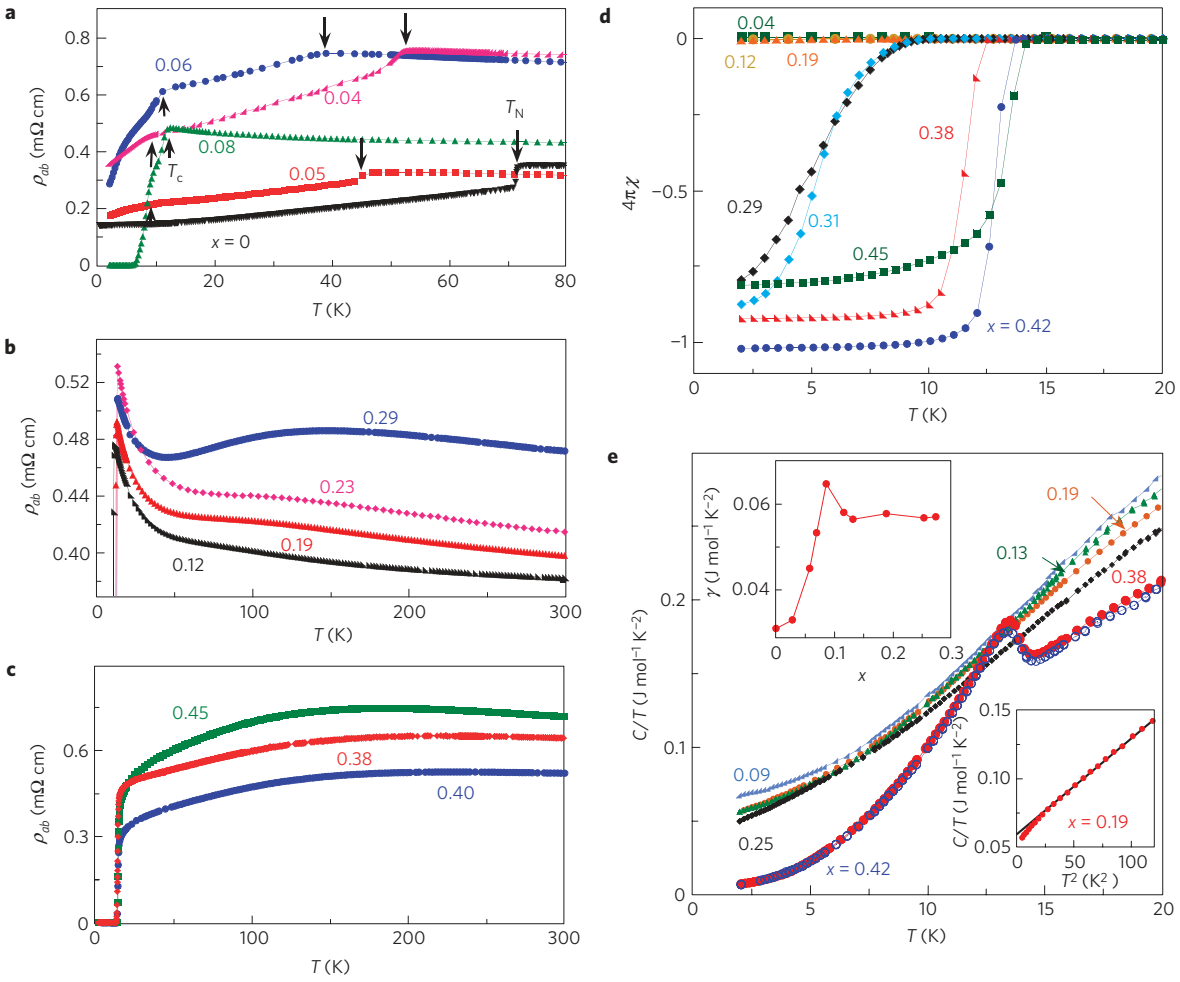

Figure 3 | Evolution of superconductivity as a function of Se content for $Fe_{1.02}(Te_{1-x}Se_x)$. **a**, In-plane resistivity $\rho_{ab}(T)$ as a function of temperature for samples in the AFM region ($0 \leq x < 0.09$). The downward arrows mark the AFM transition and the upward arrows mark the onset of a trace of superconductivity. **b**, $\rho_{ab}(T)$ for samples with $0.09 < x \leq 0.29$. **c**, $\rho_{ab}(T)$ for samples with $x > 0.29$. **d**, Magnetic susceptibility data measured with a zero-field-cooling history and a field of 30 Oe for typical samples. **e**, Specific heat divided by temperature C/T as a function of temperature for various samples. The left inset is the electronic specific heat coefficient γ as a function of Se content x. The right inset is C/T as a function of T^2 for the $x = 0.19$ sample. Both magnetic susceptibility and specific heat data show that bulk superconductivity occurs only in samples with $x \geq 0.29$. The samples with bulk superconductivity exhibit a metallic temperature dependence in ρ_{ab} in the normal state, whereas those samples without bulk superconductivity exhibit a non-metallic temperature dependence in ρ_{ab}.

data for typical samples. The electronic specific coefficient γ derived from linear fitting for various samples is given in the left inset of Fig. 3e. The right inset of Fig. 3e shows an example of the fit for the $x = 0.19$ sample where we observe a slight deviation from linearity below 4.5 K that may be due to non-bulk superconductivity. The significant increase of γ for $x \geq 0.09$ is associated with enhanced magnetic fluctuations as shown below.

In contrast, samples in region III exhibit characteristics of bulk superconductivity. Their susceptibility exhibits significant diamagnetism below T_c^{χ} and anomalous peaks near T_c^{χ} in specific heat data also indicate bulk phase transitions (see Fig. 3d,e). The inferred superconducting volume fraction rises to above 75% for $x \geq 0.29$ (Fig. 1b). In addition, samples with bulk superconductivity in region III differ from samples with non-bulk superconductivity in region II in their normal-state properties as noted above. As shown in Fig. 3b,c, the normal state in region III exhibits metallic behaviour in $\rho_{ab}(T)$. However, samples in region II show a noticeable non-metallic upturn before the superconducting transitions in $\rho_{ab}(T)$. Indeed, for $T_c < T < 20$ K, $\rho_{ab}(T)$ is characterized by a logarithmic temperature dependence (see Supplementary Information), indicating weak charge carrier localization in region II. Overall, our phase diagram in Fig. 1a is consistent with previous reports of bulk superconductivity in $Fe_{1+y}(Te_{1-x}Se_x)$ single crystals[25–27].

Why is bulk superconductivity suppressed and charge carriers weakly localized in region II? It is a critical question to understand the difference between the phase diagrams of iron chalcogenide and iron pnictide superconductors, so we examine several possible explanations in the following. One possibility is that quenched-disorder-induced charge localization suppresses superconductivity. As this is an alloy, structural disorder is present throughout regions II and III and does not readily account for the fact that bulk superconductivity occurs only in the latter region. There is however evidence that magnetic correlations are changing substantially from region II to region III. Early neutron scattering measurements revealed that whereas long-range AFM order at $(\pi,0)$ is suppressed, short-range static correlations remain near $(\pi,0)$ (refs 6,27,28). To clarify the role of such short-range magnetic correlations, we carried out neutron scattering measurements on two high-quality single-crystalline samples with $x = 0.19$ and 0.38. The $x = 0.19$ sample resides in region II and has a superconducting volume fraction of ~0.6%, whereas the $x = 0.38$ sample is in region III

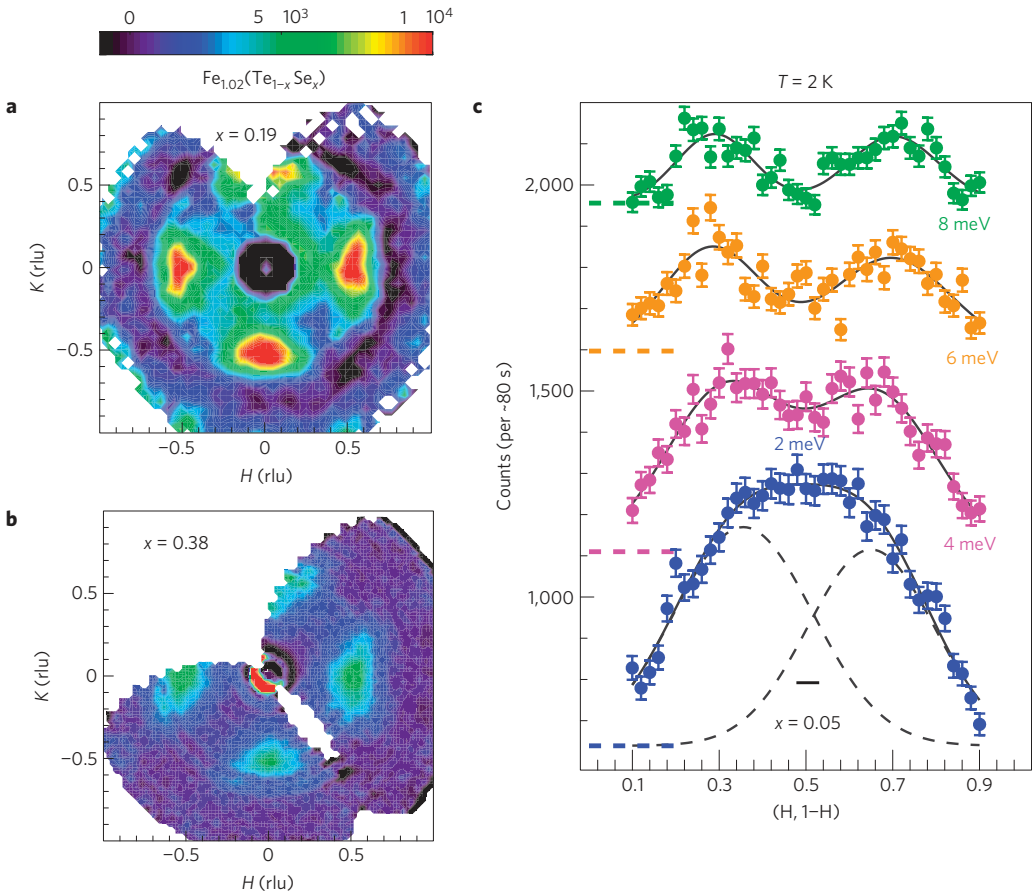

Figure 4 | Difference of microscopic magnetic properties between samples with and without bulk superconductivity. a, Neutron scattering intensity map on the (HK0) plane for the $x = 0.19$ sample without bulk superconductivity ($\hbar\omega = 0$ meV). **b**, Neutron scattering intensity map on the (HK0) plane for the $x = 0.38$ sample with bulk superconductivity ($\hbar\omega = 0$ meV). Both samples exhibit quasi-elastic scattering near (1/2, 0), but the scattering in the $x = 0.19$ sample is much stronger than that in the $x = 0.38$ sample. The data shown in **a** and **b** were measured using the multiaxis crystal spectrometer at NIST. **c**, Typical inelastic neutron scattering transverse scans through (1/2,1/2) (or (π,π)) at fixed energy measured from a single crystal of $Fe_{1.02}Te_{0.95}Se_{0.05}$ at 2 K. The solid lines through the data are Gaussian fits to the magnetic excitations. For clarity, data and fits are shifted along the *y* axis by an arbitrary amount. The position of the background for each scan is indicated by a horizontal line. The black horizontal bar represents the expected *Q*-resolution.

and has a superconducting volume fraction of ~90%. As shown in Fig. 4a,b, both samples exhibit quasi-elastic scattering centred near (π,0). With the data normalized to phonon intensity, (π,0) magnetism in the $x = 0.19$ sample is a factor of 2.3(2) stronger than in the $x = 0.38$ sample with the same correlation length of 4.4(4) Å. This short-range AFM order at (π,0) coexists with (π,π) spin fluctuations for which a spin-gap and a magnetic resonance forms for the $x = 0.38$ sample in the bulk superconducting state. For a sample with $x = 0.27$, well into region II, spin excitations at the same wave vector have been reported[29], suggesting that magnetic scattering at (π,π) and (π,0) coexist over a wide composition range.

To explore this coexistence, we carried out inelastic neutron scattering measurements on an $x = 0.05$ single crystal. This sample exhibits long-range (π,0) magnetic order with an ordered moment of 1.68(6) μ_B/Fe. In Fig. 4c we illustrate typical transverse inelastic neutron scattering scans centred at (π,π) that were measured up to 8 meV, and show the presence of well-defined magnetic excitations similar to those we reported earlier for an $x = 0.4$ sample[30]. For the lower-energy excitation at 2 meV, we find a peak with a width broader than the *Q*-resolution of the instrument. The flat-top structure suggests that it consists of two components that separate through dispersion at higher energies. As previously found for an $x = 0.4$ sample, the corresponding dispersion relation extrapolates to incommensurate points $(1/2+\varepsilon, 1/2-\varepsilon)$ with $\varepsilon = 0.10(1)$, however, with a softer dispersion velocity of 62(5) meV Å as compared with 345(2) meV Å for the $x = 0.4$ bulk superconducting sample[30].

As this is an alloy where composition and local properties must vary throughout, it is difficult to determine the length scale over which these different magnetic properties coexist in our samples. Possible situations include homogeneous, intrinsic coexistence and a two-phase description where (π,0) and (π,π) magnetic correlations exist in distinct volume fractions. It is also possible that (π,0) magnetism exists only in rare regions of the alloy as an impurity or Griffiths phase. Irrespectively, we find that bulk superconductivity occurs only when (π,0) magnetic correlations are strongly suppressed, suggesting that they are not favourable to superconducting pairing. The gradual increase of the bulk superconducting transition temperature (T_c^{χ} in Fig. 1a) and the superconducting volume fraction ($-4\pi\chi$ in Fig. 1b) with increasing Se content for $x > 0.29$ suggests that the detrimental effects of (π,0) magnetic correlations still exist in region III, progressively weakening with increasing x. A negative role for (π,0) magnetic correlations is further corroborated by our neutron scattering measurements carried out on $Fe_{1.11}(Te_{0.62}Se_{0.38})$, with excess Fe. Although the 38% Se content for $Fe_{1.02}(Te_{0.62}Se_{0.38})$ would place the sample in region III, excess Fe drives the sample into region II. Both susceptibility and specific heat measurements indicate that bulk

superconductivity is suppressed; the resistivity follows a logarithmic temperature dependence indicating weakly localized charge carriers (see Supplementary Information), consistent with our previous report[25]. Our neutron scattering measurements (see Supplementary Information) show an absence of low-energy magnetic scattering at (π,π) but clearly defined magnetic short-range ordering at (π,0). This result indicates that magnetic correlations of the (π,0) variety are destructive to superconductivity and contribute to weak charge carrier localization. For bulk superconducting samples it is at the (π,π) magnetic wave vector that a spin gap and a magnetic resonance are formed, a result consistent with $s_{\pm}$ pairing symmetry[17–19] and indicating a similar mechanism behind iron chalcogenide and iron pnictide superconductivity.

In summary, we have explored the dichotomy between (π,0) and (π,π) magnetism in the $Fe_{1.02}(Te_{1-x}Se_x)$ system. For low Se content, long-range magnetic order is formed with a magnetic wave vector (π,0). Dynamic magnetic correlations with a (π,π) wave vector however, do coexist in a wide range of the phase diagram. Increasing Se doping tunes the relative strength of these distinct correlations. Magnetic correlations near (π,0) are antagonistic to superconductivity and associated with weak charge carrier localization in an intermediate region between long-range (π,0) AFM order and superconductivity. Bulk superconductivity occurs only in a composition range where (π,0) magnetic correlations are sufficiently suppressed and (π,π) spin fluctuations associated with the nearly nesting Fermi surface dominate. This indicates that iron chalcogenide and iron pnictide superconductors, despite a competing magnetic instability in the former, have a similar mechanism for superconductivity.

Methods

$Fe_{1.02}(Te_{1-x}Se_x)$ single crystals used in this study were synthesized using a flux method[25] and were shown to be tetragonal phase with the space group $P4/nmm$ at room temperature by X-ray and neutron diffraction measurements[6]. The compositions of crystals were determined using an energy-dispersive X-ray spectrometer. As early studies revealed that the superconductivity of this system is sensitive to Fe non-stoichiometry[25,31], we have chosen samples with $y \sim 0.02$ to explore the evolution from (π,0) magnetic order to superconductivity with (π,π) magnetic resonance. We measured resistivity with a four-probe method, the Hall effect with a five-probe method and specific heat with an adiabatic relaxation technique using a commercial physical property measurement system. d.c. magnetic susceptibility was measured using a commercial superconducting quantum interference device. Neutron diffraction experiments were carried out on the four-circle diffractometer E5 and the two-axis diffractometer E4 at the BER II reactor at the Helmholtz–Zentrum, and neutron scattering measurements probing magnetic short-range order and excitations were carried out using the multiaxis crystal spectrometer and disc chopper spectrometer instruments at NIST. Inelastic neutron scattering measurements were carried out on the $x = 0.05$ sample using the triple-axis spectrometer IN8 operated by the Institut Laue-Langevin, with the sample mounted with the c axis vertical, giving us access to spin excitations within the basal ab plane.

Received 6 April 2010; accepted 8 June 2010; published online 18 July 2010

References

1. Hsu, F. C. *et al.* Superconductivity in the PbO-type structure α-FeSe. *Proc. Natl Acad. Sci. USA* **105,** 14262–14264 (2008).
2. Fang, M. H. *et al.* Superconductivity close to magnetic instability in $Fe(Se_{1-x}Te_x)_{0.82}$. *Phys. Rev. B* **78,** 224503 (2008).
3. Medvedev, S. *et al.* Electronic and magnetic phase diagram of β-$Fe_{1.01}Se$ with superconductivity at 36.7 K under pressure. *Nature Mater.* **8,** 630–633 (2009).
4. Subedi, A., Zhang, L. J., Singh, D. J. & Du, M. H. Density functional study of FeS, FeSe, and FeTe: Electronic structure, magnetism, phonons, and superconductivity. *Phys. Rev. B* **78,** 134514 (2008).
5. Xia, Y. *et al.* Fermi surface topology and low-lying quasiparticle dynamics of parent $Fe_{1+x}Te/Se$ superconductor. *Phys. Rev. Lett.* **103,** 037002 (2009).
6. Bao, W. *et al.* Tunable ($\delta\pi$, $\delta\pi$)-type antiferromagnetic order in α-Fe(Te, Se) superconductors. *Phys. Rev. Lett.* **102,** 247001 (2009).
7. de la Cruz, C. *et al.* Magnetic order close to superconductivity in the iron-based layered $LaO_{1-x}F_xFeAs$ systems. *Nature* **453,** 899–902 (2008).
8. Huang, Q. *et al.* Neutron-diffraction measurements of magnetic order and a structural transition in the parent $BaFe_2As_2$ compound of FeAs-based high-temperature superconductors. *Phys. Rev. Lett.* **101,** 257003 (2008).
9. Christianson, A. D. *et al.* Unconventional superconductivity in $Ba_{0.6}K_{0.4}Fe_2As_2$ from inelastic neutron scattering. *Nature* **456,** 930–932 (2008).
10. Lumsden, M. D. *et al.* Two-dimensional resonant magnetic excitation in $BaFe_{1.84}Co_{0.16}As_2$. *Phys. Rev. Lett.* **102,** 107005 (2009).
11. Qiu, Y. M. *et al.* Spin gap and resonance at the nesting wave vector in superconducting $FeSe_{0.4}Te_{0.6}$. *Phys. Rev. Lett.* **103,** 067008 (2009).
12. Balatsky, A. V. & Parker, D. Not all iron superconductors are the same. *Physics* **2,** 59 (2009).
13. Kamihara, Y., Watanabe, T., Hirano, M. & Hosono, H. Iron-based layered superconductor $La[O_{1-x}F_x]FeAs$ ($x = 0.05$–0.12) with $T_C = 26$ K. *J. Am. Chem. Soc.* **130,** 3296–3297 (2008).
14. Takahashi, H. *et al.* Superconductivity at 43 K in an iron-based layered compound $LaO_{1-x}F_xFeAs$. *Nature* **453,** 376–378 (2008).
15. Chen, X. H., Wu, T., Wu, G., Liu, R. H. & Fang, D. F. Superconductivity at 43 K in $SmFeAsO_{1-x}F_x$. *Nature* **453,** 761–762 (2008).
16. Rotter, M., Tegel, M. & Johrendt, D. Superconductivity at 38 K in the iron arsenide $(Ba_{1-x}K_x)Fe_2As_2$. *Phys. Rev. Lett.* **101,** 107006 (2008).
17. Mazin, I. I., Singh, D. J., Johannes, M. D. & Du, M. H. Unconventional superconductivity with a sign reversal in the order parameter of $LaFeAsO_{1-x}F_x$. *Phys. Rev. Lett.* **101,** 057003 (2008).
18. Chubukov, A. V., Efremov, D. V. & Eremin, I. Magnetism, superconductivity, and pairing symmetry in iron-based superconductors. *Phys. Rev. B* **78,** 134512 (2008).
19. Maier, T. A., Graser, S., Scalapino, D. J. & Hirschfeld, P. Neutron scattering resonance and the iron-pnictide superconducting gap. *Phys. Rev. B* **79,** 134520 (2009).
20. Zhao, J. *et al.* Structural and magnetic phase diagram of $CeFeAsO_{1-x}F_x$ and its relation to high-temperature superconductivity. *Nature Mater.* **7,** 953–959 (2008).
21. Luetkens, H. *et al.* The electronic phase diagram of the $LaO_{1-x}F_xFeAs$ superconductor. *Nature Mater.* **8,** 305–309 (2009).
22. Drew, A. J. *et al.* Coexistence of static magnetism and superconductivity in $SmFeAsO_{1-x}F_x$ as revealed by muon spin rotation. *Nature Mater.* **8,** 310–314 (2009).
23. Chen, H. *et al.* Coexistence of the spin-density wave and superconductivity in $Ba_{1-x}K_xFe_2As_2$. *Europhys. Lett.* **85,** 17006 (2009).
24. Pratt, D. K. *et al.* Coexistence of competing antiferromagnetic and superconducting phases in the underdoped $Ba(Fe_{0.953}Co_{0.047})_2As_2$ compound using X-ray and neutron scattering techniques. *Phys. Rev. Lett.* **103,** 087001 (2009).
25. Liu, T. J. *et al.* Charge-carrier localization induced by excess Fe in the superconductor $Fe_{1+y}Te_{1-x}Se_x$. *Phys. Rev. B* **80,** 174509 (2009).
26. Sales, B. C. *et al.* Bulk superconductivity at 14 K in single crystals of $Fe_{1+y}Te_xSe_{1-x}$. *Phys. Rev. B* **79,** 094521 (2009).
27. Khasanov, R. *et al.* Coexistence of incommensurate magnetism and superconductivity in $Fe_{1+y}Se_xTe_{1-x}$. *Phys. Rev. B* **80,** 140511 (2009).
28. Wen, J. *et al.* Short-range incommensurate magnetic order near the superconducting phase boundary in $Fe_{1+\delta}Te_{1-x}Se_x$. *Phys. Rev. B* **80** 104506 (2009).
29. Lumsden, M. D. *et al.* Evolution of spin excitations into the superconducting state in $FeTe_{1-x}Se_x$. *Nature Phys.* **6,** 182–186 (2010).
30. Argyriou, D. N. *et al.* Incommensurate itinerant antiferromagnetic excitations and spin resonance in the $FeTe_{0.6}Se_{0.4}$ superconductor. *Phys. Rev. B* **81,** 220503 (R) (2010).
31. McQueen, T. M. *et al.* Extreme sensitivity of superconductivity to stoichiometry in $Fe_{1+\delta}Se$. *Phys. Rev. B* **79,** 014522 (2009).

Acknowledgements

The work at Tulane is supported by the NSF under grant DMR-0645305 for materials and equipment, and the DOE under DE-FG02-07ER46358 for personnel. Work at AMRI was supported by DARPA through grant HR 0011-09-1-0047. Work at NIST is in part supported by the NSF under grant DMR-0454672. Work at the Johns Hopkins University Institute for Quantum Matter is supported by the DOE under grant DE-FG02-08ER46544. D.N.A. and K.P. acknowledge the Deutsche Forschungsgemeinschaft for support under the priority program SPP 1458 and contract AR 613/1-2.

Author contributions

T.J.L, J.H., B.Q., D.F. and Z.Q.M. carried out sample growth, transport property and specific heat measurements (T.J.L and J.H. contributed equally). Neutron scattering measurements were carried out by W.B., M.R., S.A.J.K., K.P., S.M., D.N.A., A.H., Y.Q., V.T., A.T.S., J.A.R. and C.B. Magnetic susceptibility was measured by A.R., H.P. and L.S.

Additional information

The authors declare no competing financial interests. Supplementary information accompanies this paper on www.nature.com/naturematerials. Reprints and permissions information is available online at http://npg.nature.com/reprintsandpermissions. Correspondence and requests for materials should be addressed to Z.Q.M. or W.B.